Materials Science & Engineering A 870 (2023) 144848

Contents lists available at ScienceDirect

Materials Science & Engineering A

journal homepage: www.elsevier.com/locate/msea

A high-strength precipitation hardened cobalt-free high-entropy alloy

Matthew Luebbe [a], Jiaqi Duan [a,b,*], Fan Zhang [c], Jonathan Poplawsky [d], Hans Pommeranke [a], Maalavan Arivu [a], Andrew Hoffman [a,e], Mario Buchely [a], Haiming Wen [a,f,**]

[a] Department of Materials Science and Engineering, Missouri University of Science and Technology, Rolla, MO, 65409, USA
[b] Warwick Manufacturing Group, University of Warwick, Coventry, CV4 7AL, UK
[c] Materials Measurement Science Division, National Institute of Standards and Technology, Gaithersburg, MD, 20899, USA
[d] Center for Nanophase Materials Sciences, Oak Ridge National Laboratory, TN, 37996, USA
[e] General Electric Research Center, Niskayuna, NY, 12309, USA
[f] Department of Nuclear Engineering and Radiation Science, Missouri University of Science and Technology, Rolla, MO, 65409, USA

ARTICLE INFO

Keywords:
High-entropy alloy
Precipitation strengthening
Microstructure
Mechanical properties
Strengthening mechanisms

ABSTRACT

Recent studies on precipitation-hardened high-entropy alloys (HEAs) demonstrate their high strength and thermal stability, making them promising materials for high-temperature structural applications such as nuclear reactors. However, many existing HEAs contain cobalt (Co), which is unsuitable for nuclear applications because of the long-term activation issue of Co. Co is also expensive and considered a critical material for other applications. Therefore, it is desired to exclude Co from the composition. A Co-free $(Fe_{0.3}Ni_{0.3}Mn_{0.3}Cr_{0.1})_{88}Ti_4Al_8$ HEA was developed and studied in this work. In contrast to previous Co-free HEAs, this alloy is close to equiatomic in its composition and promises a more pronounced high-entropy effect. Scanning electron microscopy, transmission electron microscopy, atom probe tomography, and synchrotron-based, high-energy X-ray diffraction were used to characterize this alloy and revealed a complex four-phase structure, with an FCC matrix, γ' precipitates, and a network of B2 and χ phase particles. This structure granted 2151 MPa compressive strength and good thermal stability, but with limited ductility and slow precipitation kinetics. A strengthening analysis of the alloy shows that the B2 and χ provided the most significant strengthening contribution, adding 312 MPa and 788 MPa respectively. The strengthening effect from the nanoscale γ′ is also considerable, adding 608 MPa in total. This study lays the foundation for the continued development of high-strength Co-free HEAs with improved and satisfactory ductility.

1. Introduction

High entropy alloys (HEAs) are alloys with multiple principal elements. They are typically defined as alloys with five or more elements with concentrations from 5 to 35 at % [1–3]. This compositional complexity can lead to severe lattice distortion, reduced diffusion kinetics, and high mixing entropy [1,4]. The existing literature has shown that HEAs possess unique properties, including high solid-solution strengthening, good thermal stability, and good ductility, as well as superior oxidation and wear resistance [5–16]. The high mixing-entropy in HEAs is supposed to promote the formation of a simple single-phase structure instead of intermetallics, and this has been intensively studied in the literature [17–23]. This single-phase (especially face-centered cubic (FCC)) structure may contribute to the high ductility commonly reported in HEAs. Meanwhile, previous studies of solid-solution FCC structured HEAs have shown disappointing strength [23–25].

Recent studies have focused on employing various strengthening mechanisms, especially precipitation strengthening [26–30] to improve the strength of these HEA systems. Through the precipitation of nanostructured phases such as B2, Laves, σ, and carbides, these alloys have shown exceptional strength [9,31–35]. For example, Gao et al. showed a strength increase of 300 MPa by introducing nanoscale NbC to a CrMnFeCoNi alloy [31]. Dasari et al. achieved a strength of 1020 MPa with 20% ductility by engineering B2 precipitation in an $Al_{0.5}Co_{1.5}CrFeNi_{1.5}$ alloy [35]. The most thorough studies have been performed on alloys with an FCC + $L1_2$ (or γ+γ′) structure similar to that observed in Ni-superalloys [26,28,30,36–39]. Two papers by He et al. reported a strength of 1100 MPa with a ductility of 40% for $(FeCoNiCr)_{94}Ti_2Al_4$.

* Corresponding author. Department of Materials Science and Engineering, Missouri University of Science and Technology, Rolla, MO, 65409, USA.
** Corresponding author. Department of Materials Science and Engineering, Missouri University of Science and Technology, Rolla, MO, 65409, USA.
E-mail addresses: Jiaqi.Duan@warwick.ac.uk (J. Duan), wenha@mst.edu (H. Wen).

https://doi.org/10.1016/j.msea.2023.144848
Received 13 December 2022; Received in revised form 22 February 2023; Accepted 24 February 2023
Available online 25 February 2023

They also experimented with other Ti and Al contents but found other compositions impaired either strength or ductility [26,36]. Yang et al. also reported γ′ precipitation in $(CoCrNi)Al_3Ti_3$ with 1300 MPa strength and 45% ductility [38]. These γ′-forming HEAs have exhibited high strength combined with good ductility, but alloy design and processing parameters must be optimized to avoid formation of embrittling intermetallics such as $L2_1$, B2, and σ [37,40]. Ti and Al are the typical additions to enhance γ′ precipitation in Ni-superalloys and existing HEAs, but they should be added in equal amounts or other Ti and Al containing intermetallics will form [40]. In addition, several papers have shown that γ′ can decay into $L2_1$ or $D0_{24}$ under certain thermo-mechanical processing conditions, impacting the mechanical properties [28,37].

In addition to increasing strength, precipitates can serve as defect sinks under irradiation, which will improve irradiation resistance [41]. The complex matrix of HEAs also improves their irradiation resistance as shown in Jin et al., in which increasing compositional complexity leads to decreased irradiation-induced swelling [42]. Precipitation-strengthened HEAs are thus expected to have improved irradiation resistance, but most HEAs studied for the irradiation resistance have been single phase [42–47]. Studies performed on irradiation of precipitation strengthened HEAs have focused on the irradiation effects on the precipitates, not the overall alloy [48]. HEAs are also commonly reported to possess good thermal stability which, when combined with good irradiation resistance, makes them promising candidate materials for critical nuclear reactor applications.

Most HEAs reported in the literature, including the high-performance γ+γ′ alloy $(FeCoNiCr)_{94}Ti_2Al_4$, contains Co [1,26]. Co activates under neutron irradiation with a half-life of ^{60}Co at ≈ 5.27 years, making its presence undesirable for nuclear reactor applications. To address this issue, precipitation hardened HEAs without Co need to be developed for crucial applications in nuclear reactors. Some HEAs without Co have already been developed, including $FeNiMnCr_{18}$ [49], non-equiatomic FeNiMnCrTiAl [27,50], the FeNiMnAl system [51], $Al_{0.5}Cr_{0.9}FeNi_{2.5}V_{0.2}$ [29,52], and $Al_{0.3}CrFe_{1.5}MnNi_{0.5}$ [53]. Several systems exhibit excellent mechanical properties and precipitation of phases such as γ′ and B2 [29,51–54]. However, many of the studied Co-free HEAs, including the best for mechanical properties and precipitation, have compositions that are far from equiatomic, such as $(FeNi)_{67}Cr_{15}Mn_{10}Ti_5Al_3$ or $Al_{0.5}Cr_{0.9}FeNi_{2.5}V_{0.2,}$ potentially impacting its solid-solution strengthening and matrix irradiation resistance [27,29,50–53,55].

According to the original HEA papers, the Cantor alloy, CoCrFeMnNi, forms a stable single-phase FCC alloy and can serve as a good basis for modifying existing compositions [3,4]. The goal of the current study was to develop an FCC+γ′ HEA without Co for nuclear applications. To achieve this goal, the existing and well-studied $(FeCoNiCr)_{94}Ti_2Al_4$ alloy was used as a basis and the Co was replaced with Mn based on the Cantor alloy. Due to the tendency of Cr to form intermetallics, especially with Mn, the concentration of Cr is also reduced, and the Ti and Al contents were increased to allow more formation of $Ni_3(Ti,Al)$ γ′ precipitates. The alloy developed and tested in this study is much closer to an equiatomic HEA than previous Co-free HEAs, leading to better overall HEA character.

2. Experimental procedures

Bulk $Fe_{26.4}Ni_{26.4}Mn_{26.4}Cr_{8.8}Ti_4Al_8$ [or $(Fe_{0.3}Ni_{0.3}Mn_{0.3}Cr_{0.1})_{88}Ti_4Al_8$] HEA samples were fabricated by vacuum induction melting of 99.9% pure elemental material. X-ray fluorescence (XRF) was performed on samples from the cast to ensure they matched the nominal composition, with the results shown in Table 1. To ensure compositional homogeneity and a starting single-phase FCC structure, the cast was homogenized at 1100 °C for 48 h in an air-filled SiC furnace inside carbon filled stainless steel bags to limit oxidation. The oxide layer formed was removed prior to aging. The homogenized sample was then sectioned and aged at 650 °C for varying durations from 0.5 h to 244 h in a box furnace. The samples were mechanically polished with a final step of 0.02 μm colloidal silica for subsequent characterization.

Table 1
Elemental composition of the overall alloy as determined by XRF compared to the nominal composition. All compositions are in atomic percent.

Element	Fe	Ni	Mn	Cr	Ti	Al
Nominal	26.4	26.4	26.4	8.8	4.0	8.0
Experimental	26.6 ± 0.2	27.3 ± 2.1	25.3 ± 2.6	8.5 ± 0.1	4.2 ± 0.1	8.1 ± 0.7

In this study, the microstructure characterization of the homogenized and peak aged samples was performed using electron backscatter diffraction (EBSD), energy dispersive spectroscopy (EDS), transmission electron microscopy (TEM), scanning transmission electron microscopy (STEM) and atom probe tomography (APT). EBSD and EDS were performed using a Helios Dual-Beam Nanolab[1] scanning electron microscope (SEM) operated at 30 kV, with a step size of 200 nm and 50 nm for the EBSD scans in Figs. 1 and 9, respectively. TEM samples were prepared using focused ion beam (FIB) lift-out on the Helios and (S)TEM characterization was performed using an FEI F20 TEM at 200 kV. The FIB on the Helios SEM was also used to mill, lift out, and thin APT tips as described by Thompson et al. [56]. APT experiments were performed using a CAMECA local electrode atom probe (LEAP 4000XHR) in laser mode with a 30K base temperature and a 50 pJ laser energy. Reconstructions were created and analyzed using CAMECA's IVAS 3.8 software.

The bulk microstructure of the alloys was also characterized using synchrotron-based X-ray diffraction measurements in transmission mode. The measurements were conducted at 9-ID-C and 11-ID of the Advanced Photon Source, Argonne National Laboratory. The X-ray wavelength was 0.5904 Å for 9-ID and 0.2113 Å for 11-ID, respectively. The photon flux at the sample was $\sim 10^{13}$ photon/mm^2/s. X-ray beam size was 800 μm × 200 μm (9-ID) and 200 μm × 200 μm (11-ID), respectively. More details about the instruments can be found elsewhere [57,58].

Hardness testing was performed using a Struers Duramin 5 Vickers hardness tester by applying a load of 4.91 N for a duration of 10 s. Tensile testing was performed using an MTS Landmark materials testing system with a 250 kN load cell. The homogenized sample was machined into tensile specimens with dimensions of 23 mm gauge length × 6.2 mm width × 5.8 mm thickness using electric discharge machining (EDM) equipment with a brass wire. The peak-aged samples proved too brittle for tensile testing and were cut into compression specimens with dimensions of 6.8 mm height × 6.4 mm × 5.8 mm cross-section. The displacement rates for tensile and compressive testing were 1.4 mm/min and 0.032 mm/min, respectively.

A CALPHAD (Calculation of Phase Diagrams) approach was used to predict and evaluate phases and their chemical compositions in the $(Fe_{0.3}Ni_{0.3}Mn_{0.3}Cr_{0.1})_{88}Ti_4Al_8$ HEA. Equilibrium CALPHAD calculations were performed using Thermo-Calc software, with a HEA database (TCHEA4). This HEA database is based on binary and ternary subsystems and the model predictions are their extrapolations for a given composition.

[1] Certain commercial products or company names are identified here to describe our study adequately. Such identification is not intended to imply recommendation or endorsement by the National Institute of Standards and Technology, nor is it intended to imply that the products or names identified are necessarily the best available for the purpose.

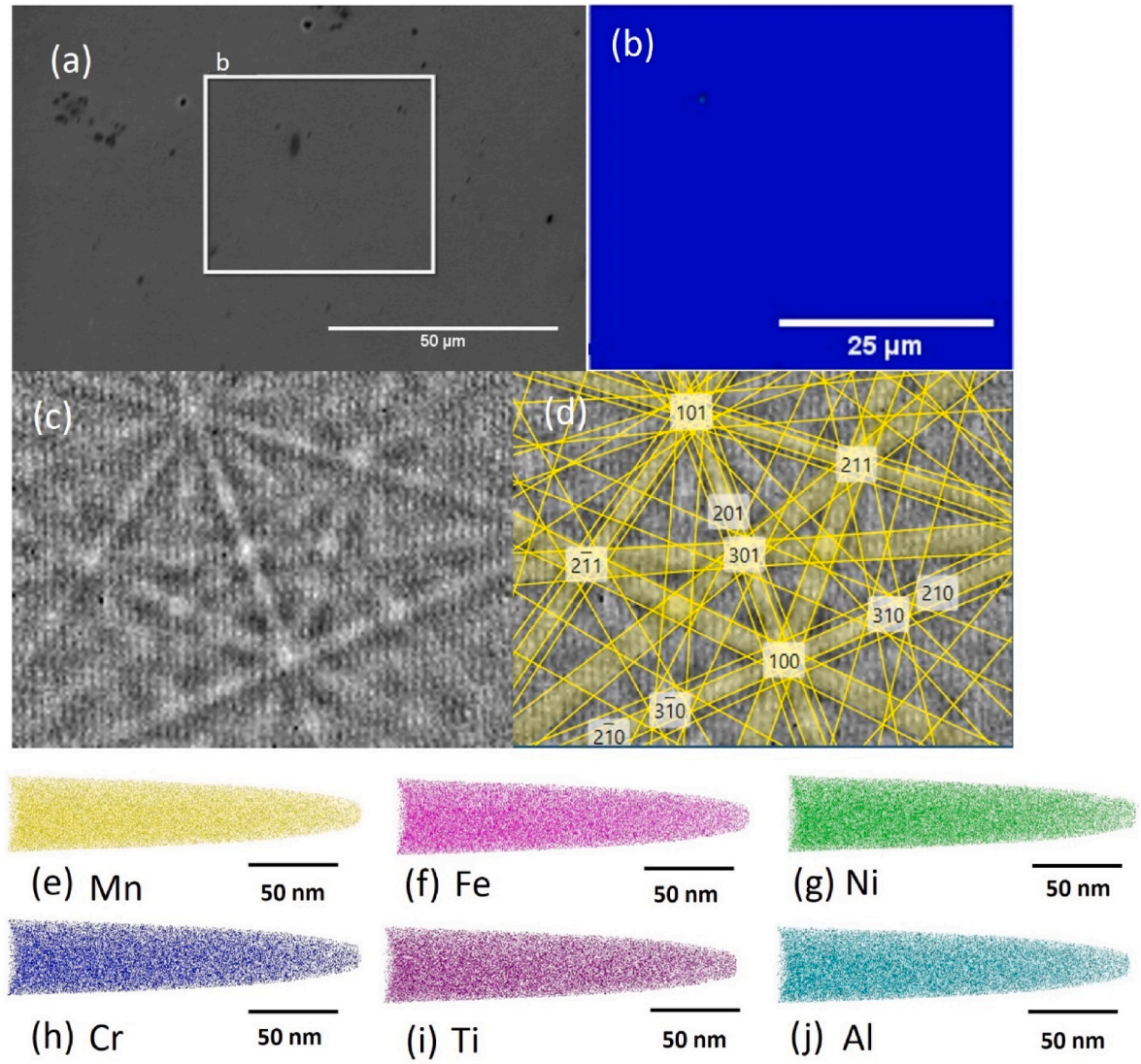

Fig. 1. $(Fe_{0.3}Ni_{0.3}Mn_{0.3}Cr_{0.1})_{88}Ti_4Al_8$ homogenized at 1100 °C for 48 h. (a) Secondary electron SEM image; (b) EBSD phase map of homogenized sample, blue corresponding to FCC iron; (c) Unindexed Kikuchi pattern and (d) indexed Kikuchi diffraction pattern (FCC). APT reconstruction atom maps of (e) Mn, (f) Fe, (g) Ni, (h) Cr, (i) Ti and (j) Al indicate compositional homogeneity. (For interpretation of the references to colour in this figure legend, the reader is referred to the Web version of this article.)

3. Results

3.1. Heat treatment

The as-cast alloy was first homogenized at 1100 °C for 48 h to ensure compositional homogeneity. To confirm that the pre-aged sample was FCC structured single-phase with no compositional variation, we used local probes such as EDS, EBSD, and APT as well as the bulk probe of synchrotron XRD on the homogenized sample. The secondary electron SEM image in Fig. 1a shows some areas that appear to be secondary phases, but the EBSD phase map, as shown in Fig. 1b, suggests that the homogenized sample is an FCC single-phase within its detection limit. The unindexed region in Fig. 1b represents TiN inclusions according to EDS taken with the map, and the overall volume fraction of the inclusions is negligible. To eliminate the possibility of misindexing by the software, Fig. 1c and d shows a Kikuchi pattern collected during the EBSD mapping, and its match after indexing respectively. Overall the indexed pattern corresponds to that of FCC iron. The atom maps also show that, within the analyzed volume, the matrix is compositionally homogeneous. The XRD data, serving as a bulk probe, indicate a dominant FCC diffraction pattern with a lattice constant of (3.640 ± 0.002) Å, shown in Fig. 2. For completeness, we note that a weak peak exists on the right shoulder of the FCC 111 peak, indicating the possibility of a secondary phase. We emphasize that this peak is the only peak detected for a possible secondary phase, and even with the high X-ray flux in a synchrotron measurement, its integrated intensity is less than 1% of that of the FCC 111 peak, proving the bulk evidence that the homogenized material is effectively a single-phase FCC alloy.

An aging study was performed to examine the evolution of material hardness as a function of aging duration and temperature. Aging temperatures which were tested are shown in Table 2, along with max hardness achieved and additional characterization performed. We experimentally determined that aging at 650 °C for 120 h represents the optimal aging condition leading to the highest strength (hardness). The hardness data after aging at 550 °C, 650 °C, and 800 °C for various duration, as shown in Fig. 3, demonstrate a wide range of materials' responses to heat treatment conditions near the optimal temperature of 650 °C.

The as-homogenized material has a Vickers hardness of 151 HV. At 650 °C, the hardness increases rapidly to 432 HV after an aging time of

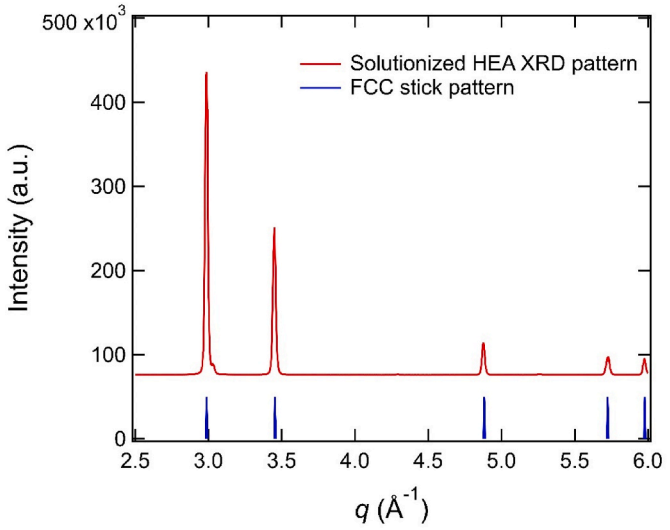

Fig. 2. Synchrotron XRD pattern of $(Fe_{0.3}Ni_{0.3}Mn_{0.3}Cr_{0.1})_{88}Ti_4Al_8$ homogenized at 1100 °C for 48 h. The pattern closely matches an FCC pattern with a lattice parameter of (3.640 ± 0.002) Å

Table 2
Aging temperatures tested in the aging study, with maximum duration, hardness and additional characterization performed listed.

Aging Temperature	Max Duration	Max Hardness	Characterization
550C	120 h	266 HV	APT
600C	72 h	452 HV	None
650C	244 h	535 HV	APT, SEM, TEM
700C	72 h	391 HV	None
750C	48 h	310 HV	None
800C	120 h	306 HV	APT, SEM

24 h. It continues to increase until 120 h of aging to a peak hardness of 535 HV. The hardness remains relatively stable, indicating that the precipitates and other phases that lead to improved hardness are thermally stable at this temperature. The slight downward trend may be related to a slow coarsening process.

At 550 °C, the hardness value increases quickly and then the rate of increase slows down. After 120 h of heat treatment at 550 °C, the material achieved a hardness of 266 HV. At 800 °C, the Vickers hardness increases rapidly to 306 HV after 12 h, at which point the hardness quickly decreases until reaching a stable value of ≈270 HV after ≈50 h. These hardness data unequivocally demonstrated that 650 °C is preferred for age hardening.

3.2. Mechanical properties

The $(Fe_{0.3}Ni_{0.3}Mn_{0.3}Cr_{0.1})_{88}Ti_4Al_8$ was mechanically tested in both the homogenized and peak-aged condition, as shown in Fig. 4. In the homogenized condition, the alloy has a yield strength of 375 MPa, an ultimate tensile strength of 746 MPa, and an elongation of 18% before failure. When aged at 650 °C for 120 h, the peak-aged alloy was too brittle for effective tensile measurements. Compression testing of pieces taken from the tensile bars was performed to evaluate the alloy strength. The sample exhibited a yield strength of 1800 MPa and an ultimate compressive strength of 2151 MPa, slightly exceeding the recorded hardness of 535 HV ~ 1750 MPa, but the compressive ductility was only (3.8 ± 0.1) %.

3.3. Microstructure after aging

3.3.1. Characterization of precipitates using EDS in SEM and TEM

We characterized the peak-aged alloy using EDS in both the SEM and TEM. A complicated microstructure of an FCC matrix and two other precipitating phases with elemental segregation were observed, as shown by the SEM data in Fig. 5. The first phase is a NiAl-enriched and FeCr-depleted B2 phase which appears lighter than the matrix under secondary electron SEM imaging. The second phase is an FeCr-enriched and NiAl-depleted χ (or Chi) phase that appears both darker than the matrix and slightly upraised from the matrix, indicating that it has a higher abrasion resistance to mechanical polishing. Notably, these two phases grow adjacent to each other in a network structure. Examples of the two phases are labeled in Fig. 5a and 5c-f. TEM data support these SEM findings, as shown in Fig. 6. The higher resolution of TEM enables elemental distribution to be more clearly observed than SEM. Specifically, while Mn appears to be homogeneous under SEM, TEM data demonstrated a slight preference for B2. Ti, which appears to be enriched in both B2 and χ under SEM, appears to show a slight preference for χ instead of B2 at a smaller scale.

Besides the B2 and χ phases, Ni_3(Ti, Al) type $L1_2$ (γ′) precipitates were also observed in the FCC matrix using APT (shown later). However, they are too small for observation in SEM, and difficult to pinpoint alongside the B2 and χ phases in TEM.

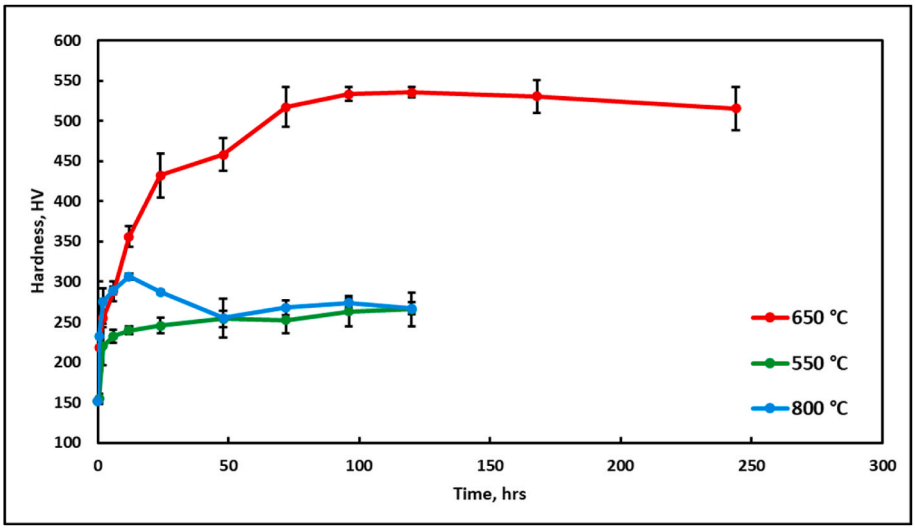

Fig. 3. Vickers microhardness of $(Fe_{0.3}Ni_{0.3}Mn_{0.3}Cr_{0.1})_{88}Ti_4Al_8$ aged at 550 °C, 650 °C, and 800 °C after homogenization.

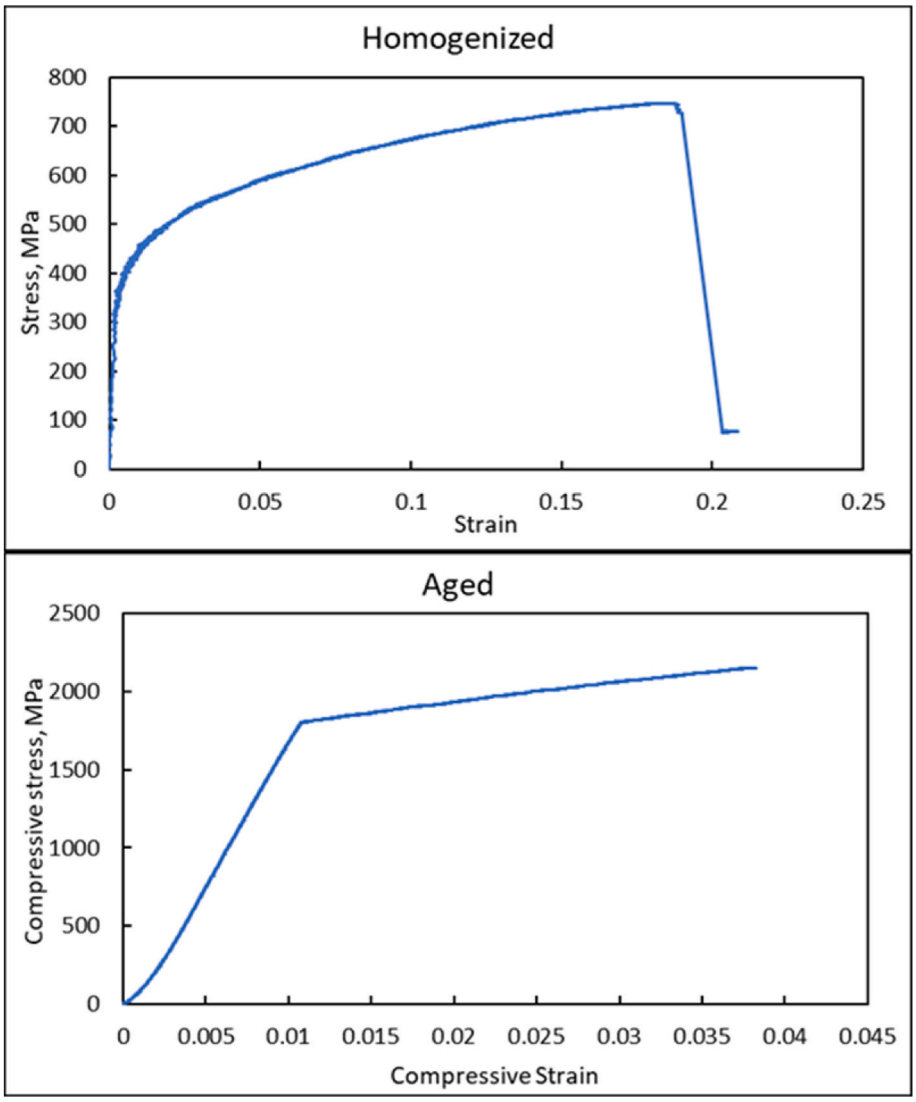

Fig. 4. Mechanical properties of $(Fe_{0.3}Ni_{0.3}Mn_{0.3}Cr_{0.1})_{88}Ti_4Al_8$ in as-homogenized state (tensile data) and aged at 650 °C for 120 h (compressive data).

3.3.2. Crystal structure and phase confirmation via diffraction techniques

To conclude that the NiAl and FeCr enriched phases were indeed B2 and χ, respectively, these phases in a peak aged sample (650 °C for 120 h) were characterized using bright-field imaging and selected-area electron diffraction (SAED) in TEM, as shown in Fig. 7. The NiAl-rich particle shown in Fig. 7b–c exhibits superstructure in the lattice expected for B2. The lattice parameter derived from the SAED pattern is 3.00 ± 0.04 Å, similar to the 2.91 Å reported in the literature for NiAl-type B2 phases [59]. In addition, the B2 phase contains a stacking structure, visible in Fig. 7a and b. This structure does not involve compositional variation, as shown in Fig. 6, and could originate from twinning previously observed in the B2 phases [60]. Fig. 7d–e shows a FeCr-rich phase particle along with its SAED pattern, indexing it as χ phase. This phase is an ordered version of α-Mn and has a lattice parameter of 8.83 ± 0.26 Å, similar to the 8.89 Å value reported for other χ-phases in the literature [61]. We also used synchrotron-based XRD to analyze the bulk structure of the alloy. The results are shown in Fig. 8. The presence of FCC (lattice parameter of a = 3.638 ± 0.002 Å), B2 (lattice parameter of a = 2.922 ± 0.002 Å), and χ (lattice parameter of a = 8.892 ± 0.006 Å) was confirmed based on XRD. The lattice parameters of each phase are very similar to those recorded in the literature but different (2.3% and 0.6% for B2 and χ, respectively) from those measured from TEM. The difference most likely originates from the calibration and collimation conditions of the TEM, and we regard the X-ray results as more accurate. Using the crystallographic information of the matrix and precipitates as input, we performed EBSD to acquire an improved understanding of the morphology and microstructure of these phases. EBSD measurements, shown in Fig. 9 demonstrate that the NiAl-rich phase is indexed as B2 phase and the FeCr indexed as χ, consistent with the TEM findings in Fig. 7.

3.3.3. Nanoscale characterization of precipitates using APT

We characterized the morphology and chemical composition of the precipitates using APT to take advantage of its sub-nm spatial resolution. Two examples, both acquired using peak-aged materials, are shown in Figs. 10–12 to highlight different phases. The APT reconstruction in Fig. 10 reveals nano-scale precipitates with diameters of about 20 nm distributed throughout the FCC matrix. These precipitates were delineated using a 40 at.% Ni iso-concentration surface (isosurface). The 3D concentration profiles across the matrix/precipitates interface indicate that the precipitates are rich in Ni and Ti, as expected for the γ' phase. An Al-rich precipitate is also present at the top of the APT tip, and the proximity histogram (proxigram) concentration profiles in Fig. 11b indicate that this precipitate is B2. A second APT reconstruction in Fig. 12 shows a χ particle rich in Fe and Cr. In addition, Fig. 12b confirms the observation from Fig. 5g that both B2 and χ phases are enriched in